Quantum Science and Technology

PAPER • **OPEN ACCESS**

Efficient microwave frequency conversion mediated by a photonics compatible silicon nitride nanobeam oscillator

To cite this article: J M Fink *et al* 2020 *Quantum Sci. Technol.* **5** 034011

View the article online for updates and enhancements.



IOP ebooks™

Bringing together innovative digital publishing with leading authors from the global scientific community.

Start exploring the collection–download the first chapter of every title for free.

This content was downloaded from IP address 151.29.243.45 on 15/06/2020 at 08:36

Quantum Science and Technology

PAPER

Efficient microwave frequency conversion mediated by a photonics compatible silicon nitride nanobeam oscillator

J M Fink[1,2,3,6], M Kalaee[1,2], R Norte[1,2,4], A Pitanti[1,2,5] and O Painter[1,2]

[1] Kavli Nanoscience Institute and Thomas J. Watson, Sr., Laboratory of Applied Physics, California Institute of Technology, Pasadena, CA 91125, United States of America
[2] Institute for Quantum Information and Matter, California Institute of Technology, Pasadena, CA 91125, United States of America
[3] Institute of Science and Technology Austria (IST Austria), 3400 Klosterneuburg, Austria
[4] Present address: Department of Precision and Microsystems Engineering, Delft University of Technology, Mekelweg 2, 2628CD Delft, The Netherlands.
[5] Present address: NEST, Istituto Nanoscienze-CNR and Scuola Normale Superiore, Piazza San Silvestro 12, 56127 Pisa (PI), Italy.
[6] Author to whom any correspondence should be addressed.

E-mail: jfink@ist.ac.at

Keywords: superconducting circuits, electromechanics, optomechanics, MEMS, frequency conversion, hybrid devices, silicon nitride membranes

OPEN ACCESS

RECEIVED
27 November 2019

REVISED
25 March 2020

ACCEPTED FOR PUBLICATION
28 April 2020

PUBLISHED
25 May 2020

Original content from this work may be used under the terms of the Creative Commons Attribution 4.0 licence.

Any further distribution of this work must maintain attribution to the author(s) and the title of the work, journal citation and DOI.

Abstract

Microelectromechanical systems and integrated photonics provide the basis for many reliable and compact circuit elements in modern communication systems. Electro-opto-mechanical devices are currently one of the leading approaches to realize ultra-sensitive, low-loss transducers for an emerging quantum information technology. Here we present an on-chip microwave frequency converter based on a planar aluminum on silicon nitride platform that is compatible with slot-mode coupled photonic crystal cavities. We show efficient frequency conversion between two propagating microwave modes mediated by the radiation pressure interaction with a metalized dielectric nanobeam oscillator. We achieve bidirectional coherent conversion with a total device efficiency of up to ~60%, a dynamic range of 2×10^9 photons/s and an instantaneous bandwidth of up to 1.7 kHz. A high fidelity quantum state transfer would be possible if the drive dependent output noise of currently $\sim$ 14 photons $s^{-1}Hz^{-1}$ is further reduced. Such a silicon nitride based transducer is *in situ* reconfigurable and could be used for on-chip classical and quantum signal routing and filtering, both for microwave and hybrid microwave-optical applications.

1. Introduction

Silicon nitride (Si_3N_4) thin films show exceptional optical and mechanical properties [1], and are used in many microelectromechanical and photonic devices. The material's large bandgap [2], high power handling due to the absence of two-photon absorption in the telecom band [3] and the low absorption losses in Si_3N_4 thin films [4] make it an ideal candidate for many photonics applications, ranging from nonlinear optics [5, 6], to atom trapping [7, 8] and tests of quantum gravity [9]. The structural stability and high mechanical quality factor [10] of high tensile stress Si_3N_4 thin films grown by low-pressure chemical vapor deposition enables nanostructures to be patterned with extreme aspect ratios [11] and form up to centimeter scale patterned membranes [12, 13] with high reflectivity [14, 15]. New soft clamping techniques make use of the tensile stress to maximize the mechanical quality factor [16–18], allowing for an unprecedented regime in which quantum coherence can be reached for micromechanical systems even in a room temperature environment [19]. Additionally, slot mode 1D photonic crystal cavities have been developed using Si_3N_4 thin films to realize strong optomechanical interactions in a small mode volume and fully integrated on-chip [20–23].

In the microwave domain, Si_3N_4 is widely used for wiring capacitors and cross-overs. Early work focused on the study of Si_3N_4 as a low loss dielectric to realize compact capacitive circuit elements operated in the quantum regime [24]; however, the amorphous material and its surface are known to host two-level defects [25], such as hydrogen impurities with sizable dipole moments and life-times, which led to the

© 2020 IOP Publishing Ltd

observation of strong coupling between a single two-level system and a superconducting resonator [26–28]. Nonetheless, due to its unique mechanical properties, high quality factor membranes [29, 30] as well as micro-machined Si_3N_4 nanobeams [31] have been coupled capacitively to superconducting resonators [32, 33] in the context of cavity electromechanics. In the latter experiments the achievable coupling strength was fundamentally limited by the small participation ratio of the motional capacitance. We recently presented a new platform that uses the membrane itself as a low loss substrate for the microwave resonator, drastically lowering the parasitic circuit capacitance and maximizing the electromechanical coupling between a metalized silicon nitride nanobeam and a high impedance superconducting coil resonator. This allowed for high cooperativities and successfully demonstrating sideband cooling of the low MHz frequency nanobeam to the motional ground state [27].

Silicon nitride membrane-based devices are currently the leading approach to couple optical and microwave systems [34, 35]. Realizing noiseless conversion with a mechanical oscillator [36–43] would allow one to build transducers for quantum networks of superconducting processors connected via resilient and low loss optical fiber networks [44–46]. Efficient wavelength conversion has been realized between optical wavelengths using silicon optomechanical crystals [47], between microwave frequencies using metallic drum resonators [48–50] and silicon nanobeams [51], and also between microwave and optical wavelength using silicon nitride membrane based Fabry–Perot cavities [34, 35] and very recently with silicon nanobeam photonic crystals [52]. Alternative approaches include the use of Josephson circuits for conversion in the microwave domain [53–56], Bragg scattering in silicon nitride rings [6] and dispersion engineering of silicon nitride waveguides [2] in the optical domain. Coupling RF and microwave fields to optics has been achieved with membranes [57, 58], via a mechanical intermediary in combination with the piezoelectric effect and optomechanical interactions [59–62], and microwave to optics conversion has been proposed [63–65] and realized with high bandwidth via the electro-optic effect [66, 67].

At room temperature wide-band microwave frequency conversion is done using commercial diode based mixers with a typical conversion loss of 6 dB. At low temperatures microwave mixing has been realized with Josephson circuits [54–56] for quantum level signals with up to 10's of MHz bandwidth and a conversion loss as low as 0.05 dB. Using parametrically driven mechanical systems for such as task typically results in lower bandwidth and potentially more noise, in particular if a low frequency intermediary is used. However, compared to Josephson circuits, mechanical transducers show orders of magnitude higher dynamic range in a more compact design with little cross-talk between mechanical modes and better resilience to stray magnetic fields. Reference [53] demonstrated mechanically mediated microwave conversion with an aluminum drum oscillator, achieving an efficiency of 95% with less than 0.1 added conversion noise quanta and a dynamic range exceeding 10^{12} photons per second over a bandwidth of 14 kHz. However, in the context of microwave to optics conversion it is not known how such metallic oscillators or Josephson circuits could be efficiently coupled to integrated photonics.

Dielectric mechanical systems offer the potential to fully separate the sensitive optical modes (superconductors cause optical loss) from the equally sensitive superconducting circuits (optical light generates quasi-particles in superconductors); for example using phononic waveguides. Our experiment is based on such a dielectric nanobeam oscillator and shares the advantages of mechanical systems compared to Josephson devices. While we do not achieve the same figures of merit as in reference [53], our experiment shows a clear path forward for coupling the dielectric mechanical intermediary to integrated photonics. The presented microwave frequency converter on the aluminum-on-Si_3N_4 platform [27], is compatible with on-chip optomechanics designs worked out in references [21, 22] and directly applicable to the low frequency silicon design in reference [52]. Compared to the latter, we anticipate that similar or improved coupling strength, transduction efficiencies and bandwidths are achievable, because the structurally stable and fully under-etched membrane design lowers the stray capacitances of the resonator inductance further [27], the techniques of soft-clamping could help to improve the mechanical quality factor [16–18], and the demonstrated V-groove based packaging can maximize fiber to chip coupling efficiencies [11]. However, high yield fabrication based on a wet release is challenging [27], the lower refractive index and dielectric permittivity compared to silicon require even smaller capacitor and slot mode gaps, and it is difficult to reliable assess the expected power handling, thermal conductivity and added noise due to optical absorption heating in a new material. A reliable quantification and comparison will therefore require careful tests at millikelvin temperatures. Nevertheless, here we show that an approach based on Si_3N_4 is feasible and promising in order to realize on-chip conversion between microwave and optical fields via radiation pressure, or to implement ultra-low voltage modulation and fully electrical tunability in Si_3N_4-based photonic devices in the near future.

2. Implementation

2.1. Physics

We realize a system where one mechanical oscillator mode with frequency $\omega_{\rm m}$ and damping rate $\gamma_{\rm m}$ is coupled to two electromagnetic resonator modes with resonance frequencies ω_i and linewidths κ_i ($i = \{1, 2\}$) via the optomechanical radiation pressure interaction as proposed in references [37–39]. In the presence of two red detuned classical drive fields $\alpha_{{\rm d},i}$ near the red sideband of the respective microwave mode at $\omega_{{\rm d},i} = \omega_i - \omega_{\rm m}$ the parametric interaction can be linearized and described by the sum of two beam splitter type interactions that allow to swap excitations between the mechanical and the two electromagnetic modes, see figure 1(a). In the resolved-sideband limit ($\omega_{\rm m} \gg \kappa_i, \gamma_{\rm m}$) the linearized electromechanical Hamiltonian in the rotating frames and the rotating wave approximation is given by

$$H = \sum_{i=1,2} \hbar\Delta_i \hat{a}_i^\dagger \hat{a}_i + \hbar\omega_{\rm m} \hat{b}^\dagger \hat{b} + \sum_{i=1,2} \hbar g_i \left(\hat{a}_i \hat{b}^\dagger + \hat{b} \hat{a}_i^\dagger \right), \tag{1}$$

where $\hat{a}_i$ is the annihilation operator for the microwave field mode, $\hat{b}$ is the annihilation operator of the mechanical mode, $\Delta_i = \omega_i - \omega_{{\rm d},i} = \omega_{\rm m}$ is the detuning between the external driving field and the relevant resonator resonance, and $g_i = g_{0,i}\sqrt{n_i}$ is the electromechanical coupling strength between the mechanical mode and resonator i with $n_i = |\alpha_{{\rm d},i}|^2 = \frac{P_{{\rm in},i}}{\hbar\omega_{{\rm d},i}} \frac{4\kappa_{{\rm ex},i}}{\kappa_i^2 + 4\Delta_i^2}$ the number of intra-resonator drive photons for the microwave input power with $P_{{\rm in},i}$.

The interaction terms of the Hamiltonian in equation (1) have two closely related effects. Optomechanical damping cools the mechanical motion with the rate $\Gamma_i = \frac{4g_i^2}{\kappa_i}$. At the same time this leads to the desired bidirectional photon conversion between two distinct electromagnetic frequencies. Using input–output theory, we can relate the itinerant input and output modes to the intra-cavity modes as $\hat{a}_{{\rm out},i} = \sqrt{\kappa_{{\rm ex},i}}\hat{a}_i - \hat{a}_{{\rm in},i}$. In the photon conversion process, an input microwave signal at frequency $\omega_{{\rm s},1}$ with amplitude $\hat{a}_{{\rm in},1}$ is down-converted to the mechanical mode at frequency $\omega_{\rm m}$, which corresponds to $\hat{b}^\dagger \hat{a}_1$ in equation (1). Next, during an up-conversion process the mechanical mode transfers its energy to the output of the other microwave resonator at frequency ω_2 and amplitude $\hat{a}_{{\rm out},2}$, which corresponds to $\hat{a}_2^\dagger \hat{b}$ in equation (1). In this process the mechanical resonance is virtually populated, in the sense that the input signal is rapidly converted to the output signal, leaving little time for the population of the intermediate mechanics. Likewise, an input microwave signal at frequency ω_2 can be converted to frequency ω_1 by reversing the conversion process, see figure 1(a). The Hermitian aspect of the Hamiltonian (1) makes this process bidirectional, without any unwanted loss, gain or noise.

We define the photon conversion efficiency via the transmission scattering parameter, i.e. as the ratio of the output-signal photon flux over the input-signal photon flux, $|S_{ij}|^2 = |\frac{\hat{a}_{{\rm out},i}}{\hat{a}_{{\rm in},j}}|^2$. By solving the linearized Langevin equations we find that for signals on resonance with the microwave resonator, in the steady state the bidirectional conversion efficiency is given as [68]

$$|S_{ij}|^2 = |S_{ji}|^2 = |T|^2 = \eta_i\eta_j \frac{4C_iC_j}{(1 + C_i + C_j)^2}, \tag{2}$$

for $i \neq j$ with $i, j = \{1, 2\}$ the indices of the two modes. $C_i = \frac{\Gamma_i}{\gamma_{\rm m}}$ is the electromechanical cooperativity for resonator i and $\eta_i = \frac{\kappa_{{\rm ex},i}}{\kappa_i}$ is the resonator coupling efficiency with $\kappa_i = \kappa_{{\rm in},i} + \kappa_{{\rm ex},i}$ the total damping rate, $\kappa_{{\rm ex},i}$ the decay rate into the waveguide and $\kappa_{{\rm in},i}$ the decay rate to any other mode. We also obtain a simple equation for the two reflection coefficients, which are given by

$$|S_{ii}|^2 = \left(1 - \frac{2\eta_i(1 + C_j)}{1 + C_i + C_j}\right)^2 \tag{3}$$

for $i, j = \{1, 2\}$ and $i \neq j$. For lossless microwave cavities $\eta_i = 1$ and in the limit $C_1 = C_2 \gg 1$ near unity photon conversion efficiency with $|T|^2 = 1$ and $|S_{11}|^2 = |S_{22}|^2 = 0$ (zero reflection) can be achieved. The former condition ($C_1 = C_2$) balances the photon–phonon conversion rates Γ_i, while the latter condition ($C_i \gg 1$) guarantees the mechanical damping rate is much smaller than the conversion rates $\gamma_{\rm m} \ll \Gamma_i$. In this limit the photon-to-photon conversion rate exceeds the mechanical damping rate—the rate at which phonons are exchanged with the noisy environment. This conversion process is coherent with the bandwidth given by $\Gamma = \gamma_{\rm m} + \Gamma_1 + \Gamma_2$, which is the total back-action-damped linewidth of the mechanical resonator in the presence of the two microwave drive fields.

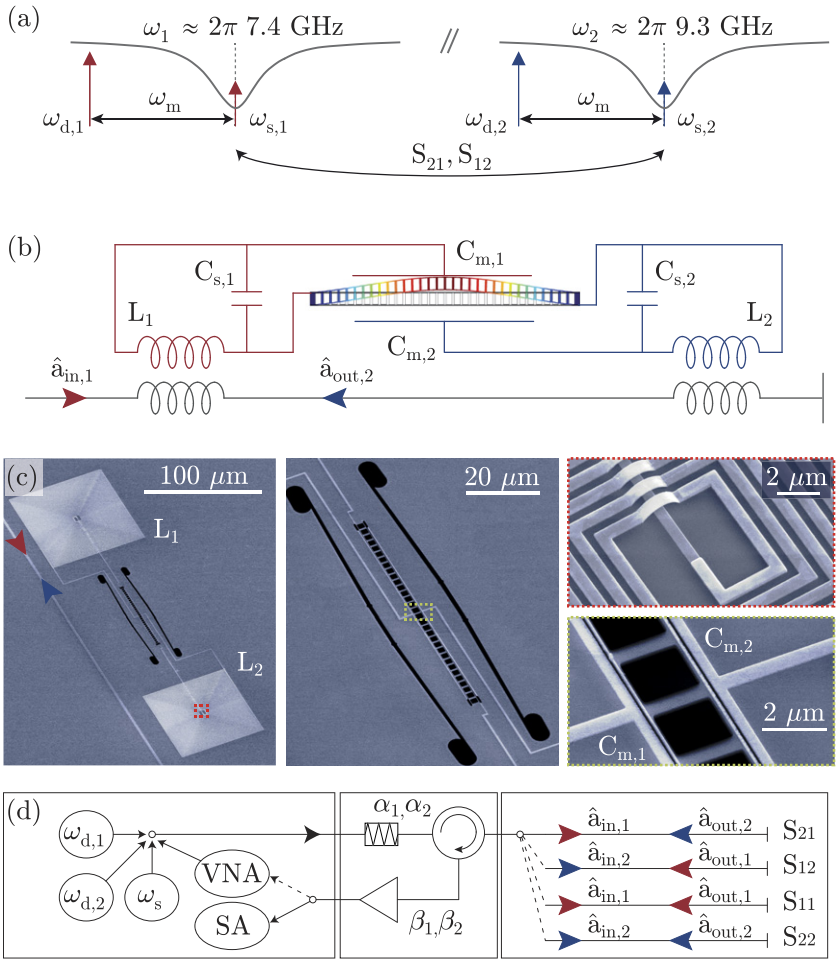


Figure 1. (a) Schematic presentation of the frequency conversion. The spectral density of the two microwave resonators at frequencies ω_i (black lines), the strong drive tones at frequencies $\omega_{d,i} = \omega_i - \omega_m$ (long red and blue arrows) and the signal tones at the optimal frequencies $\omega_{s,i} = \omega_i$ (short red and blue arrows) for $i = \{1, 2\}$, as well as the conversion scattering parameters S_{21} and S_{12} are indicated. (b) Circuit diagram of the converter. The silicon nitride nanobeam in-plane fundamental mode displacement (color indicates displacement amplitude) is coupled capacitively via its two modulated capacitances $C_{m,i}$ to two parallel inductance–capacitance resonators realized with high characteristic impedance planar spiral inductors with the inductances L_i and the stray capacitances $C_{s,i}$. The two resonant circuits are coupled inductively to a transmission line to couple in and out the propagating microwave modes $\hat{a}_{in,i}$ and $\hat{a}_{out,i}$. (c) False color scanning electron micrograph of the converter device with thin-film aluminum (white) on suspended silicon nitride membrane (blue). Mechanical beam, cross-over and capacitor region are shown enlarged. (d) Experimental setup. Three microwave sources and one vector network analyzer (VNA) output are combined at room temperature, attenuated by α_i and coupled to the device at about 12 mK using semi-rigid coaxial cables, a low loss printed circuit board and an on-chip coplanar waveguide. The reflected signals at the two frequencies of interest are routed to the output path using a cryogenic circulator and after passing another isolator (not shown) are amplified by β_i at the 4 K stage and also at room temperature before detection with either a spectrum analyzer (SA) or the VNA input.

2.2. Circuit

We implement bidirectional frequency conversion in a circuit as shown in figure 1(b). The two microwave resonators with resonance frequencies $\omega_1 = 7.444$ GHz and $\omega_2 = 9.308$ GHz are realized using two lumped element inductor–capacitor (LC) circuits formed from a planar spiral inductor of high impedance.
The capacitance of these lumped element resonant circuits is defined by the sum of the stray capacitance of the circuit, which is dominated by the inductor stray capacitance, and the mechanically modulated capacitance. The two resonators are inductively coupled to a single physical port—a 50 Ω coplanar waveguide that is shorted to ground using a thin superconducting wire close the two inductors.

2.3. Device

The described circuit is fabricated on the aluminum-on-Si_3N_4 platform similar to reference [27]. Here the entire aluminum circuit, which is shown in figure 1(c), is suspended on a fully under-etched high-stress Si_3N_4 membrane on a high resistivity silicon chip. The inductors are realized as planar spiral inductors with a pitch of 1 μm which maximizes the obtained geometric inductance per unit length, and together with the small effective permittivity of the 60 nm thin membrane, minimizes the stray capacitance of the circuit. This in turn maximizes the obtained electromechnical couplings yielding measured values of

$g_{0,1}/2\pi = 33$ Hz and $g_{0,2}/2\pi = 44$ Hz for the fundamental in-plane mechanical mode of the patterned silicon nitride nanobeam with an intrinsic damping rate of $\gamma_m/2\pi = 7$ Hz at a resonance frequency of $\omega_m/2\pi = 4.118$ MHz. This is in good agreement with calculations based on perturbation theory and electromagnetic modeling of the electric field strength at the dielectric and metallic boundaries of the vacuum gap capacitor [69]. While not measured in this work, the Si_3N_4 nanobeam has been designed as a phononic bandgap crystal that also localizes a high frequency acoustic defect mode [27]. Very recently, quantum-level transduction of hypersonic mechanical motion could be demonstrated with a similar device [70].

2.4. Setup

The experiment is performed at 12 mK inside a dilution refrigerator. At room temperature we apply the drive and signal tones with low noise microwave sources and detect both reflection scattering parameters with a vector network analyzer (VNA) and the two transmission scattering parameters with a spectrum analyzer (SA), as shown in figure 1(d). Inside the dilution refrigerator we distribute 50 Ω attenuators at various temperature stages to thermalize the electromagnetic mode temperature with the refrigerator temperature. We use one circulator to couple to the single physical port of the device in a reflection geometry. A second isolator is used to isolate the device from noise at 4 K where a commercial low noise HEMT amplifier is positioned. The four scattering parameters S_{ii} between the two mode frequencies ω_i presented in this work refer to the ratios of the 4 propagating modes in a single on-chip waveguide as schematically shown in figure 1(d).

3. Characterization

3.1. Resonators

As a first step we characterize the resonator properties using a VNA. The magnitudes of the measured complex reflection coefficients S_{ii} are normalized with $\alpha_i\beta_i \to 1$, which now corresponds to the scattering parameter at the position of the on-chip waveguide. Then the measured in-phase and quadrature phase components are fitted to the real and imaginary components of

$$S_{ii}(\omega) = e^{-i(\phi+\omega\tau)}\left(1 - \frac{\kappa_{ex,i}}{\kappa_i/2 + i(\omega_i - \omega)}\right), \tag{4}$$

where ϕ is a global phase offset and $\tau \approx 50$ ns is the delay of the signal in our setup. The result for both resonator modes are shown in figure 2(a). Here we plot the magnitude and phase of the measurement (blue points) and the fit (red lines) with excellent agreement. One can see that the resonators are both over-coupled, i.e. $\kappa_{ex,i} > \kappa_{in,i}$ as indicated by the full phase shift of $\sim 2\pi$. The comparably very high quality factors of $Q_{in,i} = \frac{\omega_i}{\kappa_{in,i}} = \{2.2 \times 10^5, 5.5 \times 10^4\}$ enable the large resonator coupling efficiencies of up to $\eta_i = \{0.92, 0.68\}$ that are essential for the efficient conversion process (cf equation (2)). In general, we find the intrinsic losses to be drive power dependent, likely due to saturation of two-level system absorption in the amorphous Si_3N_4 [24]. For the powers studied in this manuscript we determined coupling efficiencies in the range of $\eta_i = \{0.80 - 0.92, 0.54 - 0.68\}$.

3.2. Two-mode EIT

As a second step we study the reflection scattering parameters measured with a weak probe tone using the VNA in the presence of two strong red-detuned drive tones. Here we observe a variant of optomechanically induced transparency [71–73], an analog to electromagnetically induced transparency (EIT), where the mechanical sideband generated from the drives by the optomechanical interaction interfere with the weak probe tone from the VNA to modify the coherent resonator spectrum. In the case of two resonators and drive tones interacting with one mechanical mode we can model [47] and fit the measurements with

$$S_{ii}(\omega) = 1 - \frac{\kappa_{ex,i}\chi_{r,i}\left(1 + g_j^2\chi_m\chi_{r,j}\right)}{1 + \chi_m\sum_i g_i^2\chi_{r,i}} \tag{5}$$

with $i, j = \{1, 2\}$ the indices of the resonator modes, $\chi_{r,i}^{-1} = \kappa_i/2 + i(\Delta_i - \omega)$ the resonator susceptibilities and $\chi_m^{-1} = \gamma_m/2 + i(\omega_m - \omega)$ the mechanical susceptibility. Figure 2(b) shows a measurement (blue points) of the reflection scattering parameter in the vicinity of the two resonator modes together with a fit to equation (5) (red lines).

Similar to the case of standard EIT-type measurements, the formation of the peak or dip due to the mechanical mode with total linewidth Γ (as indicated in the insets of figure 2(b)) depends on the level of

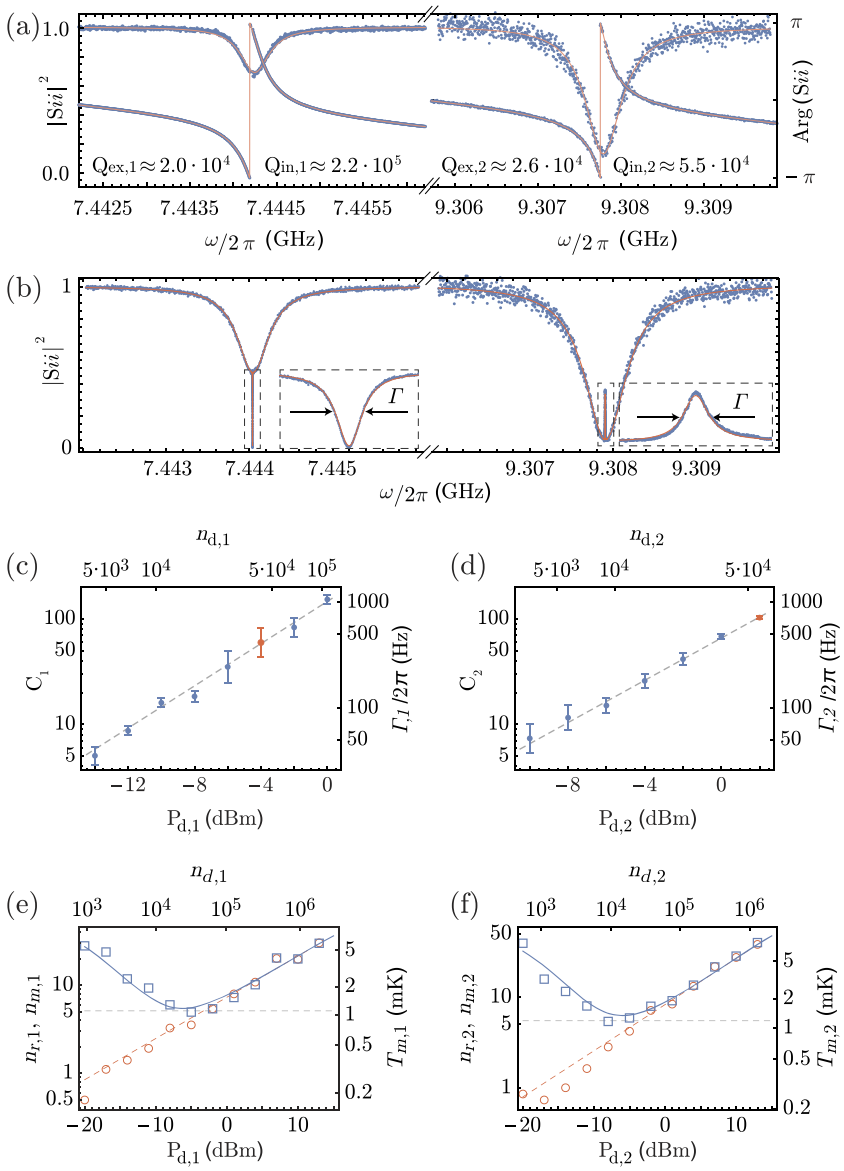


Figure 2. (a) Normalized reflected power (left axis) and phase (right axis) of a VNA measurement of the two microwave resonator modes (blue points) and a combined fit to the real and imaginary part of equation (4). The fitted extrinsic and intrinsic resonator quality factor are indicated. (b) Two-mode EIT measurement in the presence of two drive tones at $\omega_{d,1}$ and $\omega_{d,2}$ (blue points) and cred norm of equation (5) for the two microwave modes. Insets show an enlarged view in the frequency direction (boxed area of main plot) of the mechanical response with identical total linewidth Γ. (c) and (d) Fitted optomechanical damping rate Γ_i and cooperativity C_i as a function of the drive power on resonator 1 [panel (c)] and 2 [panel (d)]. Error bars show the standard deviation of the fitted cooperativity of one resonator inferred from multiple measurements with different drive powers applied to the other resonator. The data and fit shown in panel (b) was used for the data points indicated with red color. Panels (e), and (f), show the mechanical $n_{m,i}$ (blue squares) and resonator occupations $n_{r,i}$ (red circles) as well as the mechanical noise temperatures $T_{m,i}$ (right axis) as a function of red detuned drive power and the drive photon number.

cooperativity C and the degree of coupling η. However, in the present case the interpretation is more complicated because there are two terms that cause optomechanical damping. They affect each other and the double-EIT spectrum as a whole. For the chosen pump power and cooperativity combination, which is indicated in figures 2(c) and (d) by red data points, we observe a full suppression of the reflected probe signal for resonator mode 1 figure 2(b). This is a necessary condition for high efficiency conversion. In the case of resonator mode 2 on the other hand, which is only critically coupled to the waveguide ($\eta \sim 0.5$), we observe a peak in the center of the resonator, indicating a finite reflection that results in a limited conversion efficiency.

3.3. Cooperativity

We performed two-mode EIT measurements and analyses as presented above for all of the following pump power combinations: $P_{d,1}$ from −14 dBm to 0 dBm and $P_{d,2}$ from −10 dBm to 2 dBm, both in steps of 2

dB. Here the input power at the device $P_{\mathrm{in},i} = P_{\mathrm{d},i} - \alpha_i$ (on a log scale) is related to the shown drive powers via the attenuations $\alpha_i = \{69.0, 70.4\}$ dB for the two mode frequencies of interest. For each power combination we fit both spectra to a single set of parameters (specifically g_i) and summarize the results in figures 2(c) and (d). Shown are the mean and the statistical error of the cooperativities $C_i = \frac{\Gamma_i}{\gamma_\mathrm{m}}$. Using $\gamma_\mathrm{m}/2\pi = 7$ Hz obtained from cooling measurements discussed below, we also back out the optomechanical damping $\Gamma_i = \frac{4g_i^2}{\kappa_i}$ for each of the drive powers $P_{\mathrm{d},i}$, and the intra-resonator drive photon numbers $n_{\mathrm{d},i}$. We find that the dependence on drive power follows the expected behavior (dashed lines) based on the applied drive powers, attenuations and the calibrated $g_{0,i}$. The small error bars confirm that C_1 is not significantly affected by changing $P_{\mathrm{d},2}$ and vice versa. The maximum $C_{1,2} \sim 10^2$ that were obtained suggest that internal conversion efficiencies $\frac{|S_{ij}|^2}{\eta_1\eta_2} \sim 1$ can be achieved.

3.4. Sideband cooling

To estimate the noise generated by this device we perform motional sideband cooling [27, 74–77] using each resonator mode independently, i.e. with only one cooling tone at a time. The data is obtained by measuring the electronic noise spectrum due to the thermal Brownian motion of the nanobeam at the resonance frequency ω_m with the linewidth $\Gamma = \Gamma_i + \gamma_\mathrm{m}$ as a function of the cooling drive tone power $P_{\mathrm{d},i}$ applied at the optimal detuning $\Delta_i = \omega_i - \omega_\mathrm{m}$. The data shown in figures 2(e) and (f) for modes 1 and 2 has been calibrated and analyzed as described in reference [27]. For small drive photon numbers we see a decrease of the phonon occupancies $n_{\mathrm{m},i}$ (blue squares) in line with the expectations (blue lines), i.e. $n_{\mathrm{m},i} = \frac{n_\mathrm{b}}{C_i+1}$ with $n_\mathrm{b} = 60$ the mechanical bath corresponding to the refrigerator temperature of ~ 12 mK and the intrinsic mechanical linewidth γ_m (blue squares). However, we also observe a power dependent increase of the noise floor with the bandwidth of the resonator mode [33]. Using a theoretical model [27, 78] we fit the resonator occupations $n_{\mathrm{r},i}$, which we show (red circles) together with a power law fit (dashed red line) in figures 2(e) and (f). The power dependent resonator noise limits the minimum phonon occupation to $n_\mathrm{m} \sim 5$ at drive powers of about -5 dBm, independent of which resonator mode is used for cooling.

The residual thermal population of the mechanical oscillator ($n_\mathrm{m} \sim 5$) and the two microwave resonators ($n_{\mathrm{r},i} \sim 4$) leads to incoherent added noise when the device is used as a transducer. In the limit $C_1 \sim C_2 \gg 1$ and the realistic assumption that the waveguide modes are well thermalized and unpopulated, the noise added to any converted signal at the output of resonator port i is given as [49]

$$n_{\mathrm{add},i} = \eta_i(n_{\mathrm{r},1} + n_{\mathrm{r},2} + 2n_\mathrm{m}), \tag{6}$$

which results in $n_{\mathrm{add},i} \sim \{16, 12\}$ photons $\mathrm{s}^{-1}\mathrm{Hz}^{-1}$. For this estimate we have cautiously assumed the same mechanical population as measured with only a single drive tone, due to the cooling limitations imposed by the drive dependent resonator noise. In addition, finite sideband resolution could lead to gain and amplified vacuum noise. With sideband resolution factors of $\frac{\kappa_i}{4\omega_\mathrm{m}} \leqslant 10^{-3}$ this is expected to be negligible in the presented devices.

4. Wavelength conversion

4.1. Scattering parameters

In order to measure and quantify the efficiency of the wavelength converter we obtain the full set of scattering parameters for all 56 reported cooperativity combinations. The two reflection coefficients $|S_{ii}|^2$ are extracted from the center region of the two-mode EIT response shown in figure 2(b). For the transmission we apply a coherent signal on resonance with one of the two microwave resonators and measure the mechanically transduced signal appearing in the center of the other resonator using a spectrum analyzer. Measuring this in both directions allows us to calibrate the product $|S_{21}||S_{12}| = |T|^2$, i.e. the total bidirectional conversion efficiency [34], using the product of both measured off-resonant reflection coefficients $\sqrt{\alpha_1\beta_1}\sqrt{\alpha_2\beta_2} \to 1$, which were already used to normalize the reflection parameters in figures 2(a) and (b). In practice, we sweep the signal frequency in a small range δ with a span on the order of the damped mechanical linewidth and extract the maximum value of the conversion efficiency. The result is shown in figure 3(a) as a function of both cooperativities where red color indicates high and blue color indicates low values of the three scattering parameters. Qualitatively we see that matching the cooperativities leads to higher transmission and minimizes the reflection.

In panel (b) of figure 3 we show the quantitative result for the three cooperativity combinations indicated with white lines in panel (a).In the first case we show all three S parameters as a function of C_1 for $C_2 \approx 30$. As expected we observe the maximum conversion efficiency of $|S_{ij}|^2$ and the minimum reflection $|S_{ii}|^2$ for $C_1 \sim C_2$. In the second plot we fix a higher value ($C_1 \approx 95$) where we find that the optimal

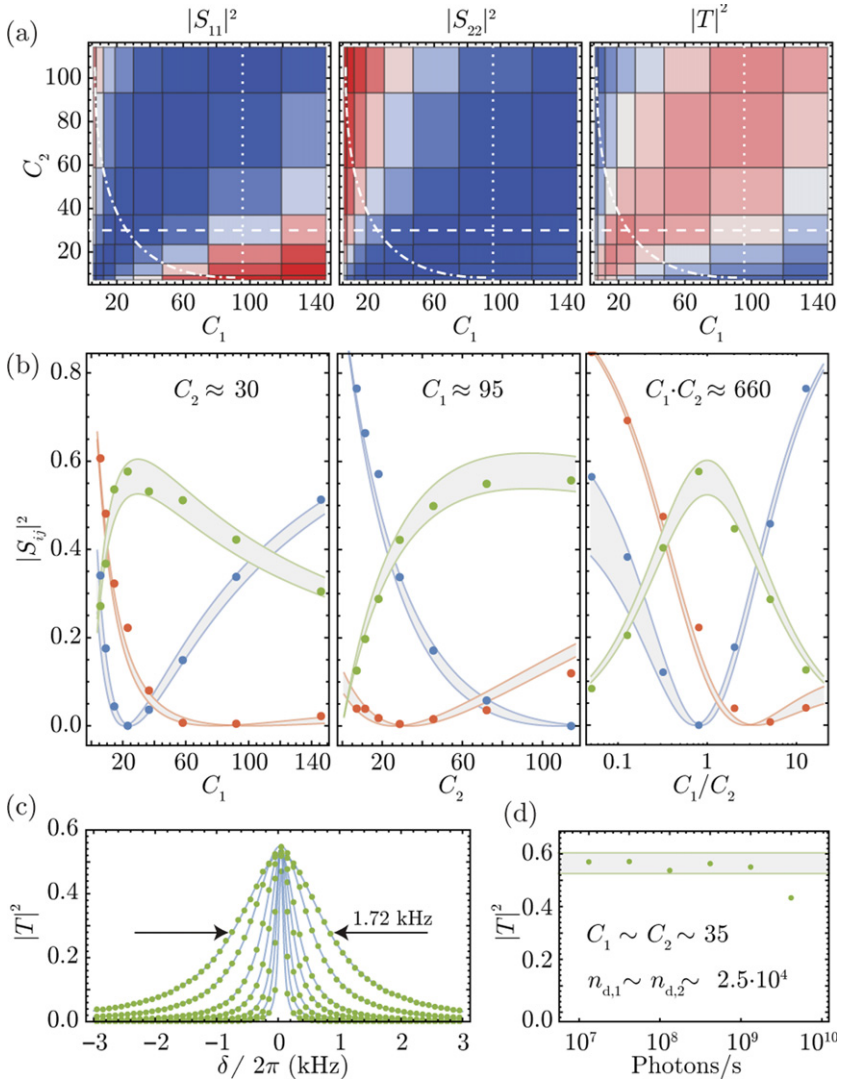


Figure 3. (a) Density plots of the two reflection and the bidirectional transmission scattering parameters (blue is low, red is high) as a function of both cooperativities C_1 and C_2. (b) Measured transmission (green dots), reflection from resonator 1 (blue dots) and resonator 2 (red dots) for the cooperativity values indicated by white lines (dashed, dotted, dashed-dotted) in panel (a). The bounds of the error bands shown (lines) are obtained from evaluating equations (2) and (3) for the minimum and maximum measured resonator coupling efficiencies of $\eta_1 = 0.85, 0.92$ and $\eta_2 = 0.64, 0.68$. (c) The measured frequency dependence of the transmission (green dots) is shown as a function of the signal detuning δ together with a Lorentzian fit (lines) for different matching cooperativities. As expected, the bandwidth $\Gamma/2\pi$ of the conversion increases with $C = C_1 = C_2$ and reaches a maximum of 1.72 kHz. (d) Dynamic range of the converter. Measured transmission as a function of the converted signal power in units of photons/s. The shaded region indicates the expected conversion efficiency for the chosen cooperativity taking into account the uncertainty in the resonator coupling efficiency.

matching condition is relaxed, i.e. the high conversion efficiency is achieved for a larger range of C_2. Finally, keeping the product constant $C_1 \times C_2 \approx 660$ and plotting the scattering parameters as a function of the ratio C_1/C_2, the matching condition $C_1 = C_2$ is very clear. Although the cooperativities are highest in the second case, the maximum conversion efficiency of $|S_{ij}|^2 \approx 0.6$ is the same due to the predicted limitations imposed by the finite resonator coupling efficiencies of $\eta_1\eta_2 \approx 0.63$. The estimated internal photon to photon conversion efficiency is $\frac{|S_{ij}|^2}{\eta_1\eta_2} \approx 0.95$. These results are in excellent agreement with the simple theory presented in equations (2) and (3) shown as solid lines in figure 3(b).

4.2. Bandwidth and dynamic range

We have seen that the conversion efficiency saturates for $C_1 = C_2 \gg 1$. The conversion bandwidth Γ on the other hand is scaling with the cooperativity. Figure 3(c) shows multiple signal frequency sweeps for different drive powers that match the cooperativity on both resonators. Here we achieve a maximum conversion bandwidth at the maximum efficiency of $\Gamma/2\pi = 1.72$ kHz. The dynamic range is tested by extracting the maximum conversion efficiency as a function of the converted signal power for $C_1 \approx C_2 \approx 35$ and the result is shown in figure 3(d). We see no significant compression up to signal levels of 2×10^9 photons/s.

5. Conclusion and outlook

In summary, we have presented a very versatile new dielectric nano-mechanical system that is suitable for efficient and near quantum limited wavelength conversion in the microwave frequency band. The unique properties of silicon nitride make it a natural platform for the realization of microwave-to-optical transducers and heralded entanglers [79]. Nevertheless, to achieve close to noise-free operation will require careful experimental tests to gain a deeper understanding of the electromagnetic and mechanical loss mechanisms, [29] and the thermal conductivity of low dimensional nano-beams [80] made from glassy materials like Si_3N_4 at temperatures in the range of only a few millikelvin [81]. This could lead to the observation of new and surprising physics along the way to fully operational quantum transducers and networks.

Acknowledgments

We thank Lukas Heinzle, Joe Redford, Marcelo Davanço, Kartik Srinivasan and Greg McCabe for help in the early parts of this work and Shabir Barzanjeh for discussions. This research was supported by the DARPA MESO program, the ARO-MURI Quantum Opto-Mechanics with Atoms and Nanostructured Diamond (Grant N00014-15-1-2761) and the Institute for Quantum Information and Matter, an NSF Physics Frontiers Center (Grant PHY-1125565) with support of the Gordon and Betty Moore Foundation. AP was supported by a Marie Curie International Outgoing Fellowship within the 7th European Community Framework Program, NEMO (GA 298861). JMF acknowledges support from the European Research Council under Grant agreement number 758053 (ERC StG QUNNECT), the Austrian Science Fund (FWF) through BeyondC (F71), an NOMIS Foundation Research Grant, and the EU's Horizon 2020 Research and Innovation Program under Grant agreement number 732894 (FET Proactive HOT).

ORCID iDs

J M Fink https://orcid.org/0000-0001-8112-028X

References

[1] Zwickl B M *et al* 2008 High quality mechanical and optical properties of commercial silicon nitride membranes *Appl. Phys. Lett.* **92** 103125
[2] Guo H *et al* 2018 Mid-infrared frequency comb via coherent dispersive wave generation in silicon nitride nanophotonic waveguides *Nat. Photon.* **12** 330–5
[3] Lacava C *et al* 2017 Si-rich silicon nitride for nonlinear signal processing applications *Sci. Rep.* **7** 22
[4] Barclay P E, Srinivasan K, Painter O, Lev B and Mabuchi H 2006 Integration of fiber-coupled high-q sin *x* microdisks with atom chips *Appl. Phys. Lett.* **89** 131108
[5] Liu Y, Davanço M, Aksyuk V and Srinivasan K 2013 Electromagnetically induced transparency and wideband wavelength conversion in silicon nitride microdisk optomechanical resonators *Phys. Rev. Lett.* **110** 223603
[6] Li Q, Davanço M and Srinivasan K 2016 Efficient and low-noise single-photon-level frequency conversion interfaces using silicon nanophotonics *Nat. Photon.* **10** 406
[7] Thompson J D *et al* 2013 Coupling a single trapped atom to a nanoscale optical cavity *Science* **340** 1202–5
[8] Yu S-P *et al* 2014 Nanowire photonic crystal waveguides for single-atom trapping and strong light-matter interactions *Appl. Phys. Lett.* **104** 111103
[9] Marshall W, Simon C, Penrose R and Bouwmeester D 2003 Towards quantum superpositions of a mirror *Phys. Rev. Lett.* **91** 130401
[10] Southworth D R *et al* 2009 Stress and silicon nitride: a crack in the Universal dissipation of glasses *Phys. Rev. Lett.* **102** 225503
[11] Cohen J D, Meenehan S M and Painter O 2013 Optical coupling to nanoscale optomechanical cavities for near quantum-limited motion transduction *Opt. Express* **21** 11227–36
[12] Duzzioni E I, Villas-Boas C J, Mizrahi S S, Moussa M H Y and Serra R M 2005 Nonadiabatic geometric phase induced by a counterpart of the stark shift *Europhys. Lett.* **72** 21–7
[13] Moura J P, Norte R A, Guo J, SchŠfermeier C and Gröblacher S 2018 Centimeter-scale suspended photonic crystal mirrors *Opt. Express* **26** 1895–909
[14] Norte R A, Moura J P and Gröblacher S 2016 Mechanical resonators for quantum optomechanics experiments at room temperature *Phys. Rev. Lett.* **116** 147202
[15] Chen X *et al* 2017 High-finesse Fabry–Perot cavities with bidimensional Si_3N_4 photonic-crystal slabs *Light: Sci. Appl.* **6** e16190
[16] Huang Y L and Saulson P R 1998 Dissipation mechanisms in pendulums and their implications for gravitational wave interferometers *Rev. Sci. Instrum.* **69** 544–53
[17] Tsaturyan Y, Barg A, Polzik E S and Schliesser A 2017 Ultracoherent nanomechanical resonators via soft clamping and dissipation dilution *Nat. Nanotechnol.* **12** 776–83
[18] Ghadimi A H *et al* 2018 Elastic strain engineering for ultralow mechanical dissipation *Science* **360** 764–8
[19] Sudhir V *et al* 2017 Quantum correlations of light from a room-temperature mechanical oscillator *Phys. Rev.* X **7** 031055
[20] Chan J, Eichenfield M, Camacho R and Painter O 2009 Optical and mechanical design of a 'zipper' photonic crystal optomechanical cavity *Opt. Express* **17** 3802–17

[21] Davanço M, Chan J, Safavi-Naeini A H, Painter O and Srinivasan K 2012 Slot-mode-coupled optomechanical crystals *Opt. Express* **20** 24394–410
[22] Grutter K E, Davanço M I and Srinivasan K 2015 Slot-mode optomechanical crystals: a versatile platform for multimode optomechanics *Optica* **2** 994–1001
[23] Norte R A, Forsch M, Wallucks A, Marinković I and Gröblacher S 2018 Platform for measurements of the Casimir force between two superconductors *Phys. Rev. Lett.* **121** 030405
[24] Paik H and Osborn K D 2010 Reducing quantum-regime dielectric loss of silicon nitride for superconducting quantum circuits *Appl. Phys. Lett.* **96** 072505
[25] Faust T, Rieger J, Seitner M J, Kotthaus J P and Weig E M 2014 Signatures of two-level defects in the temperature-dependent damping of nanomechanical silicon nitride resonators *Phys. Rev.* B **89** 100102
[26] Sarabi B, Ramanayaka A N, Burin A L, Wellstood F C and Osborn K D 2015 Cavity quantum electrodynamics using a near-resonance two-level system: emergence of the Glauber state *Appl. Phys. Lett.* **106** 172601
[27] Fink J M *et al* 2016 Quantum electromechanics on silicon nitride nanomembranes *Nat. Commun.* **7** 12396
[28] Sarabi B, Ramanayaka A N, Burin A L, Wellstood F C and Osborn K D 2016 Projected dipole moments of individual two-level defects extracted using circuit quantum electrodynamics *Phys. Rev. Lett.* **116** 167002
[29] Yuan M, Cohen M A and Steele G A 2015 Silicon nitride membrane resonators at millikelvin temperatures with quality factors exceeding 10^8 *Appl. Phys. Lett.* **107** 263501
[30] Noguchi A *et al* 2016 Ground state cooling of a quantum electromechanical system with a silicon nitride membrane in a 3D loop-gap cavity *New J. Phys.* **18** 103036
[31] Verbridge S S, Craighead H G and Parpia J M 2008 A megahertz nanomechanical resonator with room temperature quality factor over a million *Appl. Phys. Lett.* **92** 013112
[32] Regal C A, Teufel J D and Lehnert K W 2008 Measuring nanomechanical motion with a microwave cavity interferometer *Nat. Phys.* **4** 555–60
[33] Rocheleau T *et al* 2010 Preparation and detection of a mechanical resonator near the ground state of motion *Nature* **463** 72–5
[34] Andrews R W *et al* 2014 Bidirectional and efficient conversion between microwave and optical light *Nat. Phys.* **10** 321–6
[35] Higginbotham A P *et al* 2018 Harnessing electro-optic correlations in an efficient mechanical converter *Nat. Phys.* **14** 1038–42
[36] Stannigel K, Rabl P, Sørensen A S, Zoller P and Lukin M D 2010 Optomechanical transducers for long-distance quantum communication *Phys. Rev. Lett.* **105** 220501
[37] Regal C A and Lehnert K W 2011 From cavity electromechanics to cavity optomechanics *J. Phys.: Conf. Ser.* **264** 012025
[38] Safavi-Naeini A H and Painter O 2011 Proposal for an optomechanical traveling wave phonon–photon translator *New J. Phys.* **13** 013017
[39] Barzanjeh S, Abdi M, Milburn G J, Tombesi P and Vitali D 2012 Reversible optical-to-microwave quantum interface *Phys. Rev. Lett.* **109** 130503
[40] Clader B D 2014 Quantum networking of microwave photons using optical fibers *Phys. Rev.* A **90** 012324
[41] Tian L 2014 Optoelectromechanical transducer: reversible conversion between microwave and optical photons *Ann. Phys., Lpz.* **527** 1–14
[42] Zeuthen E, Schliesser A, Sørensen A S and Taylor J M 2017 Figures of merit for quantum transducers (arXiv:1610.01099)
[43] Wu M, Zeuthen E, Balram K C and Srinivasan K 2020 Microwave-to-optical transduction using a mechanical supermode for coupling piezoelectric and optomechanical resonators *Phys. Rev. Appl.* **13** 014027
[44] Kimble H J 2008 The quantum internet *Nature* **453** 1023–30
[45] Lambert N J, Rueda A, Sedlmeir F and Schwefel H G L 2020 Quantum information technologies: coherent conversion between microwave and optical photons—an overview of physical implementations *Adv. Quantum Technol.* **3** 2070011
[46] Lauk N *et al* 2020 Perspectives on quantum transduction *Quantum Sci. Technol.* **5** 020501
[47] Hill J T, Safavi-Naeini A H, Chan J and Painter O 2012 Coherent optical wavelength conversion via cavity optomechanics *Nature Commun.* **3** 1196
[48] Andrews R W, Reed A P, Cicak K, Teufel J D and Lehnert K W 2015 Quantum-enabled temporal and spectral mode conversion of microwave signals *Nat. Commun.* **6** 10021
[49] Lecocq F, Clark J B, Simmonds R W, Aumentado J and Teufel J D 2016 Mechanically mediated microwave frequency conversion in the quantum regime *Phys. Rev. Lett.* **116** 043601
[50] Ockeloen-Korppi C F *et al* 2016 Low-noise amplification and frequency conversion with a multiport microwave optomechanical device *Phys. Rev.* X **6** 041024
[51] Barzanjeh S *et al* 2017 Mechanical on-chip microwave circulator *Nat. Commun.* **8** 953
[52] Arnold G *et al* 2020 Converting microwave and telecom photons with a silicon photonic nanomechanical interface (arXiv:2002.11628)
[53] Lecocq F *et al* 2012 Coherent frequency conversion in a superconducting artificial atom with two internal degrees of freedom *Phys. Rev. Lett.* **108** 107001
[54] Abdo B *et al* 2013 Full coherent frequency conversion between two propagating microwave modes *Phys. Rev. Lett.* **110** 173902
[55] Sirois A J *et al* 2015 Coherent-state storage and retrieval between superconducting cavities using parametric frequency conversion *Appl. Phys. Lett.* **106** 172603
[56] Dmitriev A Y, Shaikhaidarov R, Antonov V N, HšAnigl-Decrinis T and Astafiev O V 2017 Quantum wave mixing and visualisation of coherent and superposed photonic states in a waveguide *Nat. Commun.* **8** 1352
[57] Bagci T *et al* 2014 Optical detection of radio waves through a nanomechanical transducer *Nature* **507** 81–5
[58] Moaddel Haghighi I, Malossi N, Natali R, Di Giuseppe G and Vitali D 2018 Sensitivity-bandwidth limit in a multimode optoelectromechanical transducer *Phys. Rev. Appl.* **9** 034031
[59] Bochmann J, Vainsencher A, Awschalom D D and Cleland A N 2013 Nanomechanical coupling between microwave and optical photons *Nat. Phys.* **9** 712–6
[60] Balram K C, Davano M I, Song J D and Srinivasan K 2016 Coherent coupling between radiofrequency, optical and acoustic waves in piezo-optomechanical circuits *Nat. Photon.* **10** 346–52
[61] Forsch M *et al* 2020 Microwave-to-optics conversion using a mechanical oscillator in its quantum ground state *Nat. Phys.* **16** 69–74
[62] Jiang W *et al* 2020 Efficient bidirectional piezo-optomechanical transduction between microwave and optical frequency *Nat. Commun.* **11** 1166

[63] Tsang M 2010 Cavity quantum electro-optics *Phys. Rev.* A **81** 063837
[64] Javerzac-Galy C *et al* 2016 On-chip microwave-to-optical quantum coherent converter based on a superconducting resonator coupled to an electro-optic microresonator *Phys. Rev.* A **94** 053815
[65] Rueda A, Hease W, Barzanjeh S and Fink J M 2019 Electro-optic entanglement source for microwave to telecom quantum state transfer *npj Quantum Inf.* **5** 108
[66] Rueda A *et al* 2016 Efficient microwave to optical photon conversion: an electro-optical realization *Optica* **3** 597–604
[67] Fan L *et al* 2018 Superconducting cavity electro-optics: a platform for coherent photon conversion between superconducting and photonic circuits *Sci. Adv.* **4** eaar4994
[68] Safavi-Naeini A H and Painter O 2011 Proposal for an optomechanical traveling wave phonon–photon translator *New J. Phys.* **13** 013017
[69] Pitanti A *et al* 2015 Strong opto-electro-mechanical coupling in a silicon photonic crystal cavity *Opt. Express* **23** 3196–208
[70] Kalaee M *et al* 2019 Quantum electromechanics of a hypersonic crystal *Nat. Nanotechnol.* **14** 334–9
[71] Weis S *et al* 2010 Optomechanically induced transparency *Science* **330** 1520–3
[72] Safavi-Naeini A H *et al* 2011 Electromagnetically induced transparency and slow light with optomechanics *Nature* **472** 69–73
[73] Teufel J D *et al* 2011 Circuit cavity electromechanics in the strong-coupling regime *Nature* **471** 204–8
[74] Marquardt F, Chen J P, Clerk A A and Girvin S M 2007 Quantum theory of cavity-assisted sideband cooling of mechanical motion *Phys. Rev. Lett.* **99** 093902
[75] Schliesser A, Rivière R, Anetsberger G, Arcizet O and Kippenberg T J 2008 Resolved-sideband cooling of a micromechanical oscillator *Nat. Phys.* **4** 415–9
[76] Chan J *et al* 2011 Laser cooling of a nanomechanical oscillator into its quantum ground state *Nature* **478** 89–92
[77] Teufel J D *et al* 2011 Sideband cooling of micromechanical motion to the quantum ground state *Nature* **475** 359–63
[78] Dobrindt J M, Wilson-Rae I and Kippenberg T J 2008 Parametric normal-mode splitting in cavity optomechanics *Phys. Rev. Lett.* **101** 263602
[79] Zhong C *et al* 2020 Proposal for heralded generation and detection of entangled microwave–optical-photon pairs *Phys. Rev. Lett.* **124** 010511
[80] Schwab K, Henriksen E A, Worlock J M and Roukes M L 2000 Measurement of the quantum of thermal conductance *Nature* **404** 974–7
[81] Hauer B D, Kim P H, Doolin C, Souris F and Davis J P 2018 Two-level system damping in a quasi-one-dimensional optomechanical resonator *Phys. Rev.* B **98** 214303